npj | 2D materials and applications

www.nature.com/npj2dmaterials

ARTICLE OPEN

Check for updates

Optical signatures of Förster-induced energy transfer in organic/TMD heterostructures

Joshua J. P. Thompson[1]✉, Marina Gerhard[1], Gregor Witte[1] and Ermin Malic[1]

Hybrid van der Waals heterostructures of organic semiconductors and transition metal dichalcogenides (TMDs) are promising candidates for various optoelectronic devices, such as solar cells and biosensors. Energy-transfer processes in these materials are crucial for the efficiency of such devices, yet they are poorly understood. In this work, we develop a fully microscopic theory describing the effect of the Förster interaction on exciton dynamics and optics in a WSe_2/tetracene heterostack. We demonstrate that the differential absorption and time-resolved photoluminescence can be used to track the real-time evolution of excitons. We predict a strongly unidirectional energy transfer from the organic to the TMD layer. Furthermore, we explore the role temperature has in activating the Förster transfer and find a good agreement to previous experiments. Our results provide a blueprint to tune the light-harvesting efficiency through temperature, molecular orientation and interlayer separation in TMD/organic heterostructures.

npj 2D Materials and Applications (2023)7:69 ; https://doi.org/10.1038/s41699-023-00430-z

INTRODUCTION

The controlled fabrication of two-dimensional heterostructures has paved the way for new cutting-edge materials and quantum technologies[1,2]. By combining materials with vastly different properties, novel device architectures can be designed to highlight and enhance desirable properties[3]. For typical, covalently bound monolayers, such as graphene, hBN and transition metal dichalcogenides (TMDs), the construction of van der Waals heterostructures has exciting physical and technological ramifications. From transistors[4,5] and superconductivity[6] to single photon emitters[7,8] and sensors[9], these structures are at the forefront of scientific development. Furthermore, more exotic combinations of materials including TMD/organic[10–13] and TMD/perovskite[14,15] heterostructures, are areas of significant interest, not just in the 2D materials community but also as a way to enhance the properties of the partner material[16].

Organic semiconductors (OSCs) have emerged as a leading candidate for a host of technological applications[17,18]. Owing to their low-cost, scalable and environmentally-friendly fabrication as well as their excellent light-harvesting properties, they are promising materials for photovoltaics[19] and sensor applications[20]. The main drawback of these materials is their low efficiency, driven, in part, by their poor mobility[21]. In a light-harvesting device, such as a solar cell, generated excitons (bound electron-hole pairs) can either recombine or separate into free charges at donor/acceptor interfaces or at the electrodes[18]. Charge separation is maximised when the mobility of the generated excitons is large allowing the charge carriers to be efficiently collected. One interesting approach to achieve this is to combine TMDs with OSCs[22]. The atomically flat interface of the TMDs acts as a good template on which to grow these crystals, and eliminates the effect of charge inhomogeneity[11]. Furthermore, depending on the band alignment of the chosen TMD and OSC, efficient charge and/or energy transfer can occur between the constituent layers. In a type-II heterostructure, charge transfer facilitates the formation of long-lived interlayer excitons[12,13,23–25]. Occurring in both type-I and -II heterostructures, energy transfer could allow excitons generated in the high absorption efficiency OSC to be transferred into the high mobility TMD[26–28]. Both these schemes represent ways to use TMDs in order to enhance the light-harvesting efficiency of an OSC.

In addition to light harvesting, TMDs have been used as detectors of organic molecules. While this can be achieved by measuring a change in the electrical signal[29,30], significant performance has been achieved using optical methods[31]. Organic molecules have been shown to modify the photoluminescence (PL) spectrum of a TMD[28,32]. An exciting proposal is to use a layer of molecular aptasensors on the TMD as a selective probe of biological and infectious compounds[33,34], such as those involved in malaria[35], cancer[36] and liver function[37]. In the absence of these compounds, energy transfer between the molecular layer and the neighbouring TMD quenches the signal of the aptasensor. At high enough concentration, the biological compound binds to the aptasensor triggering it to detach from the TMD surface and leading to a notable fluorescence/PL signal. These devices represent selective probes of target biological molecules, which could be used as ultrathin, cheap, biological sensors, not only in the laboratory but also in the home and clinical settings.

The fundamental mechanism describing the exciton energy transfer in these photovoltaic and biosensor systems is the Förster interaction[26,28], with the energy transfer commonly described as Förster-induced resonant energy transfer (FRET)[33]. Previous studies on two-dimensional systems found that the Förster interaction dominates over Dexter-mediated charge transfer processes, in spite of the sub nm separation d. This can be attributed to the deviation from the d^{-6} scaling law observed in localised molecular acceptor-donor systems, instead decaying more slowly at e^{-d} for small distances and then d^{-4} at larger distances. This was observed in graphene-TMD systems[38], TMD-single molecule[39] and molecule-graphene[40,41]. Thus, in this study, we focus on the Förster-mediated energy transfer. We develop a fully microscopic model describing the Förster interaction between an exemplary OSC/TMD heterostructure comprised of WSe_2 and tetracene. Crucially, we describe the effect of the Förster

[1]Department of Physics, Philipps-Universität Marburg, Renthof 7, 35032 Marburg, Germany. ✉email: joshua.thompson@physik.uni-marburg.de

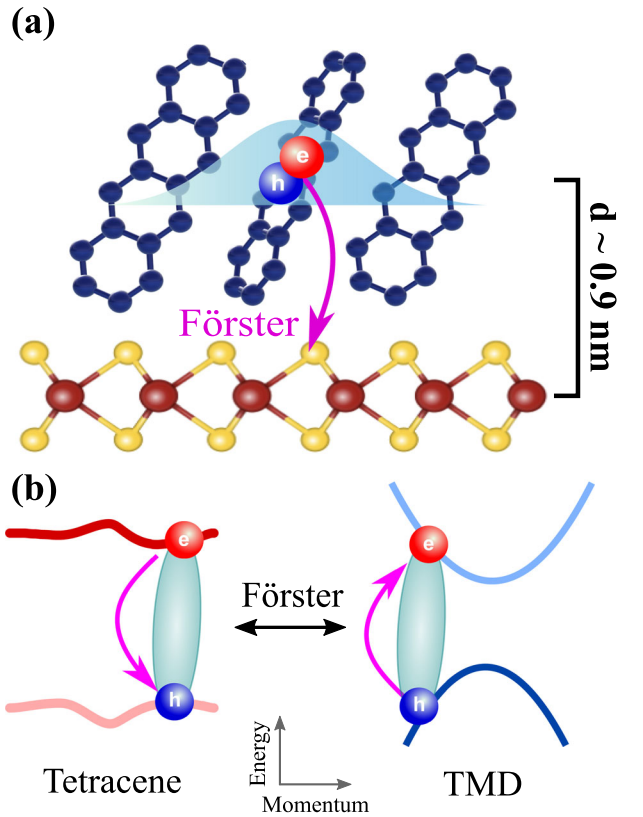

Fig. 1 Schematic of exciton energy transfer in an organic/TMD interface. a Illustration of exciton energy transfer between the tetracene (blue) and the TMD layer. **b** Single particle electronic band structure of tetracene (left) and WSe_2 (right) around the band gap. The Förster interaction, conserving energy and centre-of-mass momentum, is shown by the pink arrows.

interaction on optical spectra. We show pronounced Förster-induced signatures in differential absorption and time-resolved PL spectra. We predict a strongly unidirectional energy transfer from the organic to the TMD layer. Furthermore, we find that the transfer rate drastically increases with temperature due to the larger population of hot excitons. Our results provide a recipe with which to enhance the Förster interaction in a real heterostructure, through tuning the temperature, the interlayer distance, and the molecular orientation. By boosting the FRET in these hetero-structures, radiative losses e.g. in solar cells could be diminished, while the sensitivity of molecular aptasensors at different concentrations or orientations could be controlled.

RESULTS

Tuning of the Förster transfer rate

The Förster interaction has already been intensively studied on a microscopic footing in quantum dots[42], TMD-graphene[38] and molecule-graphene[40] systems, whereas the effect of the Förster energy transfer has not been as well understood in the technologically promising TMD/OSC heterostructures. A real space illustration of the Förster interaction is shown in Fig 1a for a tetracene/WSe_2 heterostructure. The tetracene (Tc) in its bulk polymorph can be grown on top of a WSe_2 monolayer[12,28,43].

Using the semiconductor Bloch equations and the Markov approximation[44,45], we can derive an expression for the exciton transfer rate due to the Förster interaction[38]

$$\gamma_F = \frac{2}{\hbar}\frac{1}{Z}\sum_{\eta\mathbf{Q}} \Gamma^{\eta}_{\mathbf{Q}} \exp(-E^{Tc}_{\mathbf{Q},\eta}/k_B T). \quad (1)$$

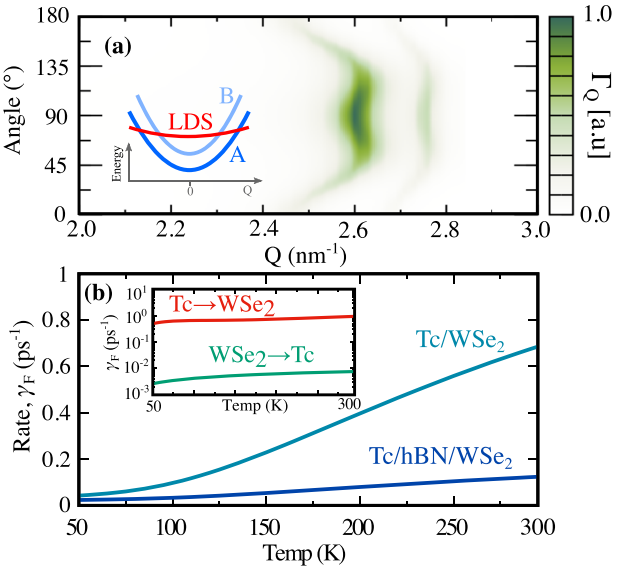

Fig. 2 Momentum and temperature dependence of Förster transfer rate. a Förster-induced exciton dephasing $\Gamma_{\mathbf{Q}}$ in the lower Davydov state of the Tc crystal as a function of momentum direction (angle) and magnitude (Q). Inset shows schematic of excitonic band structures from the A (dark blue) and B (light blue) exciton in the TMD and the lower Davydov state (red) in the Tc layer. **b** Förster-induced transfer rate from the Tc to the WSe_2 layer as a function of temperature for a direct Tc/WSe_2 interface and with an hBN spacer layer, respectively. The inset shows the temperature-dependent scattering rate both from the Tc to the WSe_2 layer (red) and from the WSe_2 to the Tc layer (green).

Here, Z is the Boltzmann partition function, such that Eq. (1) is a thermal average of the Förster dephasing rate $\Gamma^{\eta}_{\mathbf{Q}} = \pi\sum_{\mu}|V_{\mu\eta}(\mathbf{Q},z)|^2\delta(E^{Tc}_{\mathbf{Q},\eta} - E^{WSe_2}_{\mathbf{Q},\mu})$ with $V_{\mu\eta}(\mathbf{Q},z) = A^{\eta\mu}(\mathbf{Q},z)\varphi^{WSe_2*}_{\mu}(\mathbf{r}=0)\varphi^{Tc}_{,\eta}(\mathbf{r}=0)$ (c.f Methods for more details). This quantity describes exciton dephasing (and exciton linewidth broadening for $\mathbf{Q}=0$) due to the interaction of an exciton in state η in the Tc layer with momentum $\mathbf{Q}$ coupled to all states of the same momentum in state μ in the WSe_2 layer. The delta function ensures energy conservation, and coupled with the momentum and distance dependence contained in $V_{\mu\eta}(\mathbf{Q},z)$ fully determines the exciton dephasing. The reverse process (WSe_2 to Tc) can be obtained by taking the thermal average over the TMD states. Our approach allows us to track not only the layer which excitons reside in, but also their momentum. This is crucial given that the excitons with higher momentum are precisely those which engage in the Förster energy transfer. As such, our model is more accurate than typical rate-equation-based approaches[26].

In Fig. 2a, the exciton dephasing of the lowest Davydov state is shown as a function of the center-of-mass momentum magnitude Q and angle. The anisotropy of the Tc band structure gives rise to the characteristic shape of the intense region in (a), while the intensity varies in part due to the dipole orientation. The optical dipole of the lower Davydov state (LDS) is y-polarised (90°), aligned along the **a**-axis of the tetracene[46], and hence the strongest dephasing is observed in this orientation. This dipole dependence also explains the vanishing intensity at orthogonal angles (0° and 180°). The two distinct bands appearing in Fig. 2a originate from the coupling between the LDS in Tc and the A and B excitons in the TMD layer. The stronger emission stems from the coupling with the B exciton, which occurs at lower momenta as energy conservation occurs at lower Q for this pair of bands. This can be seen in the inset of Fig. 2a, where the intersection of the excitonic dispersion (representing momentum and energy

conservation) determines the shape of the features in Fig. 2a. In other many-particle processes, such as exciton-phonon scattering, the dephasing rate Γ leads to a broadening of the exciton linewidth in PL and absorption spectra. In Förster processes, however, this dephasing vanishes at $Q = 0$ corresponding to the light-cone.

Previous experimental studies have estimated the Förster transfer rate, demonstrating a net transfer of excitons from a Tc layer into a WSe_2 layer[28] with a transfer time of approximately 3 ps corresponding to a transfer rate of ~0.29 ps^{-1}. This occurs on a timescale much slower than typical exciton phonon-relaxation times in the material[47], but also quicker than singlet fission and charge transfer[28]. Evaluating Eq. (1), we calculate the temperature dependence of the exciton transfer rate γ_F from the Tc to the WSe_2 layer, cf. Fig. 2b. We distinguish two cases: Tc directly on WSe_2 (light blue) and including an hBN spacer layer (dark blue). As the temperature increases, the population of higher momentum excitons increases. Since it is precisely these excitons that participate in the Förster transfer process (note the linear Q dependence in Eq. (3)), the scattering rate also increases with temperature. Adding additional hBN or organic spacer layers allows to tune the interlayer distance z. We recover a z^{-4} dependence at large distances, characteristic of 2D systems[38,40], while at shorter distances a more rapid exponential decay is found. As a result, we find a lower Förster rate (~5 × lower) in presence of a hBN spacer layer, cf. Fig. 2b. This finding suggests that even in a multilayer Tc system, the main Förster interaction occurs between the WSe_2 and the Tc layer at the interface. This and the fact that Tc excitons are strongly confined to individual Herringbone Tc layers[46] suggests that our results can be extended to multi-layer Tc on WSe_2. In the inset of Fig. 2b, we compare the Förster transfer rate for exciton transfer from the Tc to WSe_2 (red) and the WSe_2 to the Tc (green), with the former being around two orders of magnitude larger. The relatively flatter electronic and hence excitonic bands in the Tc crystal lead to a broader momentum occupation and hence higher population of Tc excitons at larger **Q**. As a result, the Förster-mediated exciton transfer is much larger from the Tc to the WSe_2 layer than the other way round. We therefore predict a strong net transfer of excitons from the organic to the TMD layer.

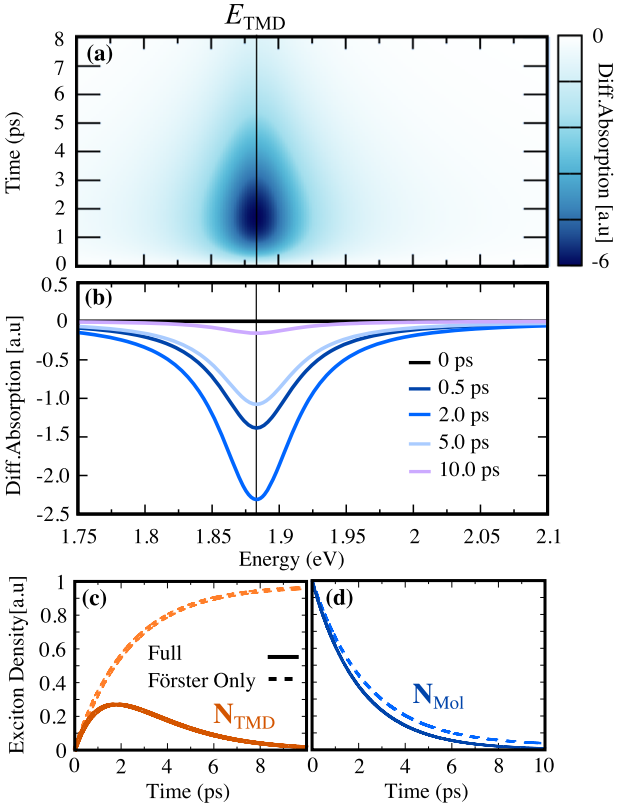

Fig. 3 Impact of Förster on time-resolved differential absorption. **a** Time-resolved differential absorption spectrum of the WSe_2 layer at 300 K. The lowest 1s exciton resonance is shown by the vertical line. **b** Time cuts of the differential absorption. Temporal evolution of the exciton density in the (**c**) TMD and the (**d**) Tc layer, taking into account the full dynamics (solid) and without the radiative loss (dashed).

Förster visualized in differential absorption

The most convenient way to track the exciton transfer due to the Förster interaction is by employing optical spectroscopy techniques. The spectroscopy of choice should allow the population in one or both layers to be tracked. In differential absorption we can directly visualize the population change in either layer[48–50]. The exciton absorption can be described using the well-established Elliot formula[44,45]

$$I_\omega(t) = \sum_\mu \frac{(1 - B^\mu(t))|M_\mu|^2}{\left(E_{0,\mu}^{WSe_2} - \hbar\omega\right)^2 + \left(\gamma_\mu + \Gamma_\mu^{phon}\right)^2} \quad (2)$$

where γ_μ and Γ_μ^{phon} are the radiative and non-radiative (phonon) decay rates, respectively. The exciton-photon light-matter interaction M_μ, is reduced by the bleaching term $B^\mu = \sum_{\mathbf{K},\mu',\mathbf{q}} N_{\mathbf{K}}^{\mu'}(|\varphi_{\mathbf{q}+\beta_{\mu'}\mathbf{K}}^{\mu'}|^2 + |\varphi_{\mathbf{q}-\alpha_{\mu'}\mathbf{K}}^{\mu'}|^2)|\varphi^\mu(\mathbf{r}=0)|^{-1}\varphi_{\mathbf{q}}^\mu$ where $\alpha^\mu = m_c^\mu/M$ and $\beta^\mu = m_v^\mu/M$. This term crucially depends on the time-dependent excitonic population $N_K^{\mu'}$. We assume the optical excitation to be weak, such that the Coulomb renormalization of the excitonic resonance[48–50] is negligible and bleaching dominates. At much larger excitation fluences, clear resonance shifts should be observed due to population-induced screening and band renormalisation, while the bleaching term can become larger than 1, leading to optical gain.

We derive a set of coupled semiconductor Bloch equations for the exciton polarization and incoherent exciton density, to describe this process (see SI for more details). We take explicitly into account in- and out-scattering between the incoherent excitons in the two layers due to both Förster and exciton-phonon scattering. The excitonic properties, calculated using the Wannier equation, in addition to the phonon properties, allow us to determine not only the scattering dynamics but also the exciton broadening appearing in Eq. (2). The differential absorption $\Delta I_\omega(t) = I_\omega(t) - I_\omega(0)$ is defined as the difference in the absorption at time t after excitation, and before the excitation $t = 0$. It is shown for a WSe_2/Tc heterostructure in Fig 3a. At time $t = 0$, the differential absorption is 0 by definition. However, following an excitation pulse resonantly exciting the Tc layer at $t = 0$, the generated excitons transfer via the Förster coupling to the WSe_2 layer. The phonon-driven intraband relaxation processes are, however, much faster than the Förster interaction[38,47], such that excitons in each layer remain thermalised. Using thermal averages, we find a simpler model for the exciton dynamics in the TMD ($l = 0$) and Tc ($l = 1$) layer

$$\partial_t N^l = -\gamma_{loss}^l N^l - \gamma_F^l N^l + \gamma_F^{1-l} N^{1-l} \quad (3)$$

such that in the bleaching term described above we define $N_{\mathbf{Q}}^{\mu l}$ as $N_{\mathbf{Q}}^{\mu l} = \frac{N^l}{Z}\exp(-E_{\mathbf{Q},\mu}^l/k_BT)$. The first term in Eq. (3) describes the radiative and non-radiative loss[45] scaling with the decay rate γ_{loss}. The second and third term describe the Förster-induced out- and in-scattering, respectively. These equations are accurate when the Förster transfer occurs on a longer timescale than the phonon-scattering rate.

In Fig. 3a, we find a negative differential absorption of WSe_2 for times $t > 0$, which is a result of the energy transfer from the Tc to the layer. This signature corresponds to the filling and hence

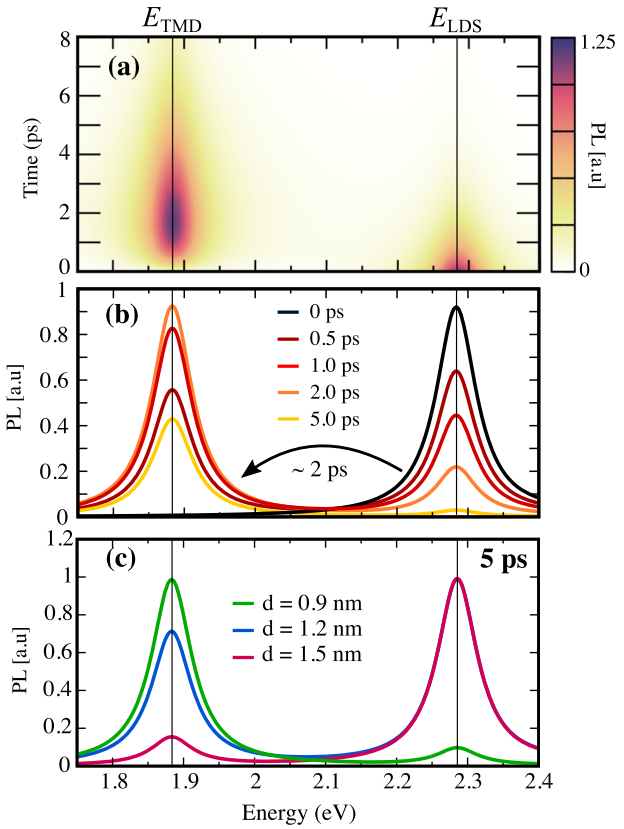

Fig. 4 Impact of Förster and interlayer separation on time-resolved photoluminescence. a Time- and energy-resolved photoluminescence spectrum of the WSe_2 and Tc layer at 300 K. The 1s exciton resonance in the TMD and the lower-Davydov state in the Tc layer are marked by vertical lines, respectively. **b** Snapshots of the PL at constant times, with an arrow marking the trend of exciton transfer due to the Förster interaction. **c** PL spectra at 5 ps for different interlayer distances.

bleaching of the 1s A exciton in WSe_2. Signatures of the B exciton, can be seen in the absorption (cf. SI), however, due to the rapid phonon-mediated relaxation of the B exciton, this bleaching is much smaller and not resolvable on the same scale.Time cuts show a characteristic dip, cf. Fig. 3b. The differential absorption decreases between $t = 0$ ps to around $t = 2$ ps owing to the build-up of excitons on the TMD layer. After around 2 ps, a steady state is reached between the exciton population in the WSe_2 and the one in the Tc layer, such that the decrease in the exciton population in both layers is driven primarily by the radiative and non-radiative decay. The temporal evolution of the exciton populations in the TMD and molecular layer are shown in Fig. 3c and d, respectively. We find that the population in the TMD layer initially increases before it drops, while the population of the Tc layer monotonously decreases. For the population in the TMD, we find an interplay of Förster-induced energy transfer from the TC layer (population increases) and the radiative exciton recombination (population decreases). This results in a maximum population around 2 ps, cf. Fig. 3c. In the absence of radiative recombination, we find a complete exciton transfer from the Tc to the WSe_2 layer (dashed lines). The pronounced dip in the differential absorption is a clear indication of the Förster-induced energy transfer. The specific distance dependence of the Förster interaction (z^{-4} as explicitly shown in the SI) compared to other processes, such as tunneling or Dexter transfer[40], allows us to identify the microscopic origin of the differential absorption signatures.

Förster visualized in time-resolved PL

An additional probe of the Förster-induced exciton dynamics can be achieved by using time-resolved photoluminescence[13,45]. As in the previous case, the LDS exciton in the Tc layer is resonantly excited leading to a thermalised exciton distribution on a short time-scale (<1 ps)[47]. The dynamics of the relative populations follow the results outlined in Fig. 3c and d. The time-resolved PL is proportional to the exciton population within the light cone, $N_0^{\mu_l l}$, and is described using the Elliot formula for PL[45]

$$I_\omega^{\mathrm{PL}}(t) = \sum_{\mu_l, l} \frac{N_0^{\mu_l l} |M_{\mu_l}^{l}|^2}{\left(E_{0,\mu_l}^{\mathrm{l}} - \hbar\omega\right)^2 + \left(\gamma_{\mu_l} + \Gamma_{\mu_l}^{\mathrm{phon}}\right)^2} \tag{4}$$

summing the contributions from both layers l. This equation differs from the aborption as it direcly depends on the exciton population $N^{\mu_l l}$. The PL spectra are shown in Fig. 4a as a surface plot displaying the time and energy dependence. At time $t = 0$, the exciton population is primarily in the Tc layer, so a clear signature of the lower Davydov state is observed. After around 1 ps, the Förster energy transfer occurs, depleting the signature from the LDS and leading to a pronounced increase in the PL of the A exciton in the WSe_2 layer. Time snapshots are shown in Fig. 4b. We estimate an energy transfer time of around 1–2 ps, which can be observed in the PL emission originating from the WSe_2 reaching a maximum at around this time. We observe again how the PL signal begins to decrease after around 2 ps due to the exciton loss due to radiative and non-radiative decay. Differences in the decay rates will not change the qualtitative predictions and will only alter the time at which the strongest signal is observed, both in the PL and the differential absorption. To demonstrate how the PL spectra are affected by the interlayer separation between the WSe_2 and Tc layers, we show in Fig. 4c, the normalised PL spectra at the fixed time of 5 ps for different interlayer distances d. For a typical distance of $d = 0.9$ nm (green line), most of the excitation has transferred from the Tc to the TMD layer, leading to a strong quenching of the molecular PL peak. When the distance is increased, however, the exciton transfer rate significantly decreases (cf Fig. 2b and SI) and the dominant PL signal stems from the Tc exciton (pink and blue lines). Approximately 60% of the PL signal comes from the molecular LDS exciton for $d = 1.2$ nm (blue), increasing to over 90% for 1.5 nm separation (pink). This demonstrates the sensitivity of this system to the interlayer distance, which can be tuned e.g. through hBN spacer layers or exploited in organic/TMD aptasensors.

DISCUSSION

Depending on the structural geometry, namely the separation between the organic and TMD layers, different spectroscopic methods may be better suited to observe the Förster-mediated energy transfer. When the interlayer separation is small, the rate is larger and higher-resolution methods, will be more appropriate to track the population transfer, which will occur on shorter timescales. Differential absorption, typically measured using pump-probe typically has sub-picosecond time resolution[51], and is therefore preferential over time-resolved PL. Similarly, in the case of one or more spacer layers or lower temperatures, time-resolved PL may be better suited, which typically has picosecond or longer time-resolution[51]. This is because a higher time-resolution is less important when the the Förster interaction is weakened at larger interlayer distances, as the slower exciton transfer is only observable over a longer timescale. This can be observed in Fig. 4c, where even after 5 ps there is little transfer between the organic and TMD layers, when the interlayer separation grows.

The Förster coupling could be technologically exploited. The observed strong quenching of the PL signal from the molecular

crystal is the crucial mechanism behind many optical biosensors[33,35]. Here, in the absence of the target molecule, the signature from the aptasensor adsorbed on the TMD is efficiently quenched. When a target molecule is present, the sensing molecules forming the molecular crystal, detach from the surface. This increases the molecular distance from the TMD, causing the Förster coupling to quickly decrease, such that the molecular PL or fluorescence signal is no longer quenched. The sensitivity of this sensing technique is evident in Fig. 4c, where for only a small increase in the interlayer separation (from 0.9 nm to 1.5 nm), the molecular PL signal goes from almost entirely quenched to almost completely unquenched, after 5 ps. The coverage of molecules and the energetic/spatial separation between the molecular and TMD excitons allow the sensitivity of a biosensor to be tuned. Closer energetic alignment between exciton resonances will lead to even stronger exciton quenching. In our case, we used a well-known, exemplary organic crystal, however, our model can be easily extended to other organic molecules. Furthermore, an organic crystal is not strictly necessary, and similar results should be expected with a more sparse covering of molecules on the TMD. The competition with temperature should also allow for a thermally-activated biosensor. Anisotropic materials, such as the Rhenium TMDs[52], could also allow the orientation of the organic molecules relative to the TMD to be detected, due to the requirement that the TMD and organic dipoles should be aligned[27]. In the same vein, the "handedness" of chiral molecules could also be distinguished in the optical spectra[53], provided the Förster interaction occurs on a shorter timescale than the intervalley relaxation in the TMD.

In this work, we presented microscopic insights into the Förster interaction between TMDs and organic crystals. We developed a fully-microscopic model describing the energy transfer and its optical signatures in a heterostructure composed of an organic semiconductor crystal and TMD monolayers. Focusing on the exemplary WSe_2/Tc heterostructure, we show a characteristic temperature and distance dependence of the Förster-induced dephasing and exciton transfer. We estimate the energy transfer time and find a good agreement with previous experimental studies. The main message of this work lies in the question of how Förster processes manifest in the optical spectra of an organic/TMD heterostructure. We demonstrate that the time-resolved differential absorption and photoluminescence can capture the Förster-driven exciton dynamics well, by tracking the change in the exciton population in the constituent layers. Our work represents a significant advance in the microscopic understanding of organic/TMD interfaces and energy-transfer processes therein, important for fundamental physics but also for the design of new optoelectronic devices, such as biosensors.

METHODS

Microscopic model for Förster transfer

Following optical excitation, the generated electron-hole pairs interact via the screened Coulomb interaction forming excitons[54]. We use the Wannier equation[44] to calculate the exciton energy dispersion $E^{\mathrm{WSe_2\,(Tc)}}_{\mathbf{Q},\nu}$ and the corresponding excitonic wavefunctions $\varphi^{\mathrm{WSe_2\,(Tc)}}_{\mathbf{k},\nu}$. The Wannier equation has been effective in determining the excitonic binding energy in previous calculations on tetracene and pentacene, with a good agreement to experiments[47]. This is further justified by the fact that the excitonic wavefunction in oligoacenes, such as tetracene and pentacene, is dispersed over multiple neighbouring molecules and hence resembles a localised Wannier exciton[46,47,55,56].

In tetracene, the symmetrically distinct molecules in the unit cell gives rise to a Davydov splitting of the excitonic state[46]. After photoexcitation, the exciton can then recombine, thermalise via scattering with phonons[47], undergo the so-called singlet fission forming two long-lived triplet excitons[18,57] and in the heterostructure case, take part in charge and energy transfer processes between the Tc and WSe_2 layers. Charge transfer, mediated by tunnelling/hopping processes,[25] gives rise to the formation of interlayer excitons. However, this requires a significant wavefunction overlap, which is reduced in the considered herringbone structure, due to the relatively large interlayer separation of 0.9 nm[28]. Furthermore, in the considered heterostructure Tc/WSe_2, the band alignment is such that charge transfer processes occur on a much slower time scale[28] and hence the optically darker interlayer excitons are not expected to significantly contribute to optics nor the dynamics[13].

On the other hand, the Förster interaction depends less strongly on the interlayer separation[38,40], involving energy transfer between intralayer excitons in the constituent layers (cf. Fig. 1a). In momentum space, the Förster interaction involves the recombination (annihilation) of an exciton (electron and hole pair) in one layer and the creation of an exciton in other layer, mediated by the Coulomb interaction[38]. The Hamiltonian describing this process in the Tc/WSe_2 heterostructure can be written as,

$$H_F = \sum_{\substack{\lambda,\lambda',\nu,\nu' \\ \mathbf{k},\mathbf{k}',\mathbf{q},\mathbf{q}'}} V^{\mathbf{k},\mathbf{k}',\mathbf{q},\mathbf{q}'}_{\lambda,\lambda',\nu,\nu'} \hat{a}^{\dagger}_{\lambda,\mathbf{k}} \hat{B}^{\dagger}_{\nu,\mathbf{q}} \hat{B}_{\nu',\mathbf{q}'} \hat{a}_{\lambda',\mathbf{k}'} + h.c, \tag{5}$$

where $\hat{a}^{(\dagger)}$ and $\hat{B}^{(\dagger)}$ are annihilation (creation) operators acting on the Tc and WSe_2 layer, respectively. The indices λ and ν describe the hybrid spin/valley/band index. The Coulomb matrix element $V^{\mathbf{k},\mathbf{k}',\mathbf{q},\mathbf{q}'}_{\lambda,\lambda',\nu,\nu'}$ is screened by the surrounding dielectric, ϵ, of a SiO_2 substrate[28]. Using a real-space coordinate transformation the Coulomb matrix element is $V^{\mathbf{k},\mathbf{k}',\mathbf{q},\mathbf{q}'}_{\lambda,\lambda',\nu,\nu'} = \sum_{\mathbf{sQ}} e^{-i\mathbf{Q}(\mathbf{s}+\mathbf{z})} \delta_{\mathbf{Q},\mathbf{k}-\mathbf{k}'} \delta_{\mathbf{Q},\mathbf{q}'-\mathbf{q}} I^{\mathbf{s},\mathbf{z}}_{\mathbf{k},\mathbf{q},\mathbf{Q}}$, where $I^{\mathbf{s},\mathbf{z}}_{\mathbf{k},\mathbf{q},\mathbf{Q}}$ takes the form of a dipole-dipole interaction (cf. the SI), separated into in-plane, $\mathbf{s}$, and out-of-plane, $\mathbf{z}$, components.

Since the dominant Förster transfer processes occur between the lowest lying energy levels, we consider only the highest valence/lowest conduction band with the same spin, while the WSe_2 and the HOMO/LUMO of the Tc. We only consider spin-like states, as the Coulomb matrix elements vanish for excitons comprised of opposite spins[58]. The same applies to momentum dark intervalley excitons in both layers[54]. In the tetracene layer, the upper and lower Davydov excitons originate from the intermolecular coupling between the symmetrically distinct molecules in the unit cell. The resulting lower and upper Davydov excitons form around the M and Γ point respectively[46]. Taking this into account, we arrive at the Förster Hamilton operator in the excitonic basis (see the SI for a detailed derivation)

$$H_F = \sum_{\eta,\mu,\mathbf{Q}} A^{\eta\mu}(\mathbf{Q},z) \varphi^{\mathrm{WSe_2}\,*}_{\mu} \varphi^{\mathrm{Tc}}_{\eta} \hat{X}^{\mathrm{WSe_2}\,\dagger}_{\mathbf{Q}\mu} \hat{X}^{\mathrm{Tc}}_{\mathbf{Q}\eta} + h.c. \tag{6}$$

where $\hat{X}^{l\,(\dagger)}_{\mathbf{Q}\mu}$ are exciton annihilation (creation) operators with momentum $\mathbf{Q}$, and energy level μ, on layer l. Here, we can express the excitonic wavefunction in real-space coordinates as $\sqrt{A}\varphi_{\mu/\eta}(\mathbf{r}=0) = \sum_{\mathbf{k}} \varphi_{\mathbf{k},\mu/\eta}$, were the hybrid indices λ, ν have been absorbed in the excitonic indices μ and η. The appearing matrix element $A^{\eta\mu}(\mathbf{Q},z)$ can be expressed analytically (cf. the SI).

$$A^{\eta\mu}(\mathbf{Q},z) = \frac{e^{-iQ_z z} e^{-|z|Q}}{4\epsilon_0 \epsilon} \mathbf{d}^{\mathrm{WSe_2}} \cdot \mathbf{Q}\left(\frac{\mathbf{Q}}{|\mathbf{Q}|} + i\hat{z}\right) \cdot \mathbf{d}^{\mathrm{Tc}}. \tag{7}$$

Here, we have introduced the optical transition dipoles $|\mathbf{d}^{\mathrm{WSe_2}}| = 0.4$ nm[38] and $|\mathbf{d}^{\mathrm{Tc}}| = 0.05$[59] and are assumed to be approximately constant around the WSe_2 and Tc valleys, respectively[38]. The out-of-plane unit vector $\hat{z}$ and out-of plane momentum Q_z also appear in the the dipole-dipole interaction, and become more relevant in structures with organic dipoles pointing perpendicularly to the layer plane.

Encoded in this Hamiltonian is the conservation of the center-of-mass momentum between the excitons in the WSe_2 and Tc. This is shown schematically in Fig. 1b. Importantly, the matrix element $A(\mathbf{Q}, z)$ describes the dependence on the exciton momentum and interlayer separation z. We find that the Förster interaction vanishes as $\mathbf{Q} \to 0$, which is typical for dipole-dipole-type coupling. The transition dipole of the TMD is circularly polarised, with handedness depending on the valley, which give rise to the well-known optical valley selection rules in TMDs[60]. In contrast, the lowest Davydov excitons in Tc are linearly polarised[59,61]. As a result the Förster matrix element becomes anisotropic in $\mathbf{Q}$, favouring the transition dipole of the initial or final Davydov exciton. Unless otherwise stated, we take a typical interlayer separation of 0.9 nm, defined as the distance between the W-atom layer in the middle of the WSe_2, and the centre of Tc layer (c.f. Fig. 1a).

DATA AVAILABILITY

The data presented was generated from the mathematical algorithm outlined in the main text, methods and Supplementary Information. The data that support the findings of this study are available from the corresponding author upon reasonable request.

CODE AVAILABILITY

The code used to generate the results of this study is available from the corresponding author upon reasonable request.

Received: 14 March 2023; Accepted: 4 September 2023;
Published online: 21 September 2023

REFERENCES

1. Geim, A. K. & Grigorieva, I. V. Van der Waals heterostructures. *Nature* **499**, 419–425 (2013).
2. Liu, Y. et al. Van der Waals heterostructures and devices. *Nat. Rev. Mater.* **1**, 1–17 (2016).
3. Mueller, T. & Malic, E. Exciton physics and device application of two-dimensional transition metal dichalcogenide semiconductors. *npj 2D Mater. Appl.* **2**, 1–12 (2018).
4. Wang, X. et al. Van der Waals negative capacitance transistors. *Nat. Commun.* **10**, 1–8 (2019).
5. Leech, D. J., Thompson, J. J. P. & Mucha-Kruczyński, M. Negative differential resistance in Van der Waals heterostructures due to moiré-induced spectral reconstruction. *Phys. Rev. Appl.* **10**, 034014 (2018).
6. Cao, Y. et al. Unconventional superconductivity in magic-angle graphene superlattices. *Nature* **556**, 43–50 (2018).
7. Yu, H., Liu, G.-B., Tang, J., Xu, X. & Yao, W. Moiré excitons: from programmable quantum emitter arrays to spin-orbit–coupled artificial lattices. *Sci. Adv.* **3**, e1701696 (2017).
8. Baek, H. et al. Highly energy-tunable quantum light from moiré-trapped excitons. *Sci. Adv.* **6**, eaba8526 (2020).
9. Kim, Y. et al. 2D transition metal dichalcogenide heterostructures for p-and n-type photovoltaic self-powered gas sensor. *Adv. Funct. Mater.* **30**, 2003360 (2020).
10. Bettis Homan, S. et al. Ultrafast exciton dissociation and long-lived charge separation in a photovoltaic pentacene–MoS2 van der Waals heterojunction. *Nano Lett.* **17**, 164–169 (2017).
11. Huang, Y. L. et al. The organic–2D transition metal dichalcogenide heterointerface. *Chem. Soc. Rev.* **47**, 3241–3264 (2018).
12. Zhu, T. et al. Highly mobile charge-transfer excitons in two-dimensional WS2/tetracene heterostructures. *Sci. Adv.* **4**, eaao3104 (2018).
13. Thompson, J. J. P. et al. Interlayer exciton landscape in WS_2/tetracene heterostructures. *Nanoscale* **15**, 1730–1738 (2023).
14. Shi, E. et al. Two-dimensional halide perovskite nanomaterials and heterostructures. *Chem. Soc. Rev.* **47**, 6046–6072 (2018).
15. Karpińska, M. et al. Interlayer excitons in MoSe 2/2D perovskite hybrid heterostructures–the interplay between charge and energy transfer. *Nanoscale* **14**, 8085–8095 (2022).
16. Lin, Y. et al. 17% efficient organic solar cells based on liquid exfoliated WS2 as a replacement for PEDOT: PSS. *Adv. Mater.* **31**, 1902965 (2019).
17. Wilson, M. W. et al. Ultrafast dynamics of exciton fission in polycrystalline pentacene. *J. Amer. Chem. Soc.* **133**, 11830–11833 (2011).
18. Congreve, D. N. et al. External quantum efficiency above 100% in a singlet-exciton-fission–based organic photovoltaic cell. *Science* **340**, 334–337 (2013).
19. Darling, S. B. & You, F. The case for organic photovoltaics. *RSC Adv.* **3**, 17633–17648 (2013).
20. Lee, Y. H. et al. Recent advances in organic sensors for health self-monitoring systems. *J. Mater. Chem. C* **6**, 8569–8612 (2018).
21. Moser, M., Wadsworth, A., Gasparini, N. & McCulloch, I. Challenges to the success of commercial organic photovoltaic products. *Adv. Energy Mater.* **11**, 2100056 (2021).
22. Sun, J. et al. 2D–organic hybrid heterostructures for optoelectronic applications. *Adv. Mater.* **31**, 1803831 (2019).
23. Jiang, Y., Chen, S., Zheng, W., Zheng, B. & Pan, A. Interlayer exciton formation, relaxation, and transport in TMD van der Waals heterostructures. *Light Sci. Appl.* **10**, 1–29 (2021).
24. Ovesen, S. et al. Interlayer exciton dynamics in van der Waals heterostructures. *Commun. Phys.* **2**, 1–8 (2019).
25. Schmitt, D. et al. Formation of moiré interlayer excitons in space and time. *Nature* **608**, 499–503 (2022).
26. Kozawa, D. et al. Evidence for fast interlayer energy transfer in MoSe2/WS2 heterostructures. *Nano Lett.* **16**, 4087–4093 (2016).
27. Gu, J. et al. Dipole-aligned energy transfer between excitons in two-dimensional transition metal dichalcogenide and organic semiconductor. *ACS Photonics* **5**, 100–104 (2018).
28. Ye, L. et al. Ultrafast singlet energy transfer before fission in a Tetracene/WSe2 Type II hybrid heterostructure. *J. Phys. Chem. Lett.* **12**, 8440–8446 (2021).
29. Wang, B. et al. Gate-modulated high-response field-effect transistor-type gas sensor based on the MoS2/Metal–organic framework heterostructure. *ACS Appl. Mater. Interfaces* **14**, 42356–42364 (2022).
30. Kumar, Y. R., Deshmukh, K., Kovářík, T. & Pasha, S. K. A systematic review on 2D materials for volatile organic compound sensing. *Coord. Chem. Rev.* **461**, 214502 (2022).
31. Feierabend, M., Berghäuser, G., Knorr, A. & Malic, E. Proposal for dark exciton based chemical sensors. *Nat. Commun.* **8**, 1–6 (2017).
32. Feierabend, M. et al. Molecule signatures in photoluminescence spectra of transition metal dichalcogenides. *Phys. Rev. Mater.* **2**, 014004 (2018).
33. Zhou, J., Chen, J., Ge, Y. & Shao, Y. Two-dimensional nanomaterials for Förster resonance energy transfer–based sensing applications. *Nanophotonics* **9**, 1855–1875 (2020).
34. Sen, R. K. et al. 2D materials-based aptamer biosensors: present status and way forward. *Curr. Med. Chem.* **29**, 5815–5849 (2022).
35. Geldert, A. et al. Paper-based MoS2 nanosheet-mediated FRET aptasensor for rapid malaria diagnosis. *Sci. Rep.* **7**, 1–8 (2017).
36. Kong, R.-M., Ding, L., Wang, Z., You, J. & Qu, F. A novel aptamer-functionalized MoS2 nanosheet fluorescent biosensor for sensitive detection of prostate specific antigen. *Anal. Bioanaly. Chem.* **407**, 369–377 (2015).
37. Shanmugaraj, K. & John, S. A. Water-soluble MoS2 quantum dots as effective fluorescence probe for the determination of bilirubin in human fluids. *Spectrochim. Acta A Mol. Biomol. Spectrosc.* **215**, 290–296 (2019).
38. Selig, M., Malic, E., Ahn, K. J., Koch, N. & Knorr, A. Theory of optically induced Förster coupling in van der Waals coupled heterostructures. *Phys. Rev. B* **99**, 035420 (2019).
39. Katzer, M. et al. Impact of dark excitons on Förster-type resonant energy transfer between dye molecules and atomically thin semiconductors. *Phys. Rev. B* **107**, 035304 (2023).
40. Malic, E., Appel, H., Hofmann, O. T. & Rubio, A. Forster-induced energy transfer in functionalized graphene. *J. Phys. Chem. C* **118**, 9283–9289 (2014).
41. Swathi, R. & Sebastian, K. Distance dependence of fluorescence resonance energy transfer. *J. Chem. Sci.* **121**, 777–787 (2009).
42. Richter, M. et al. Theory of excitation transfer in coupled nanostructures–from quantum dots to light harvesting complexes. *Phys. Status Solidi B* **243**, 2302–2310 (2006).
43. Hummer, K. & Ambrosch-Draxl, C. Electronic properties of oligoacenes from first principles. *Phys. Rev. B* **72**, 205205 (2005).
44. Kira, M. & Koch, S. W. Many-body correlations and excitonic effects in semiconductor spectroscopy. *Prog. Quantum Electron.* **30**, 155–296 (2006).
45. Brem, S., Selig, M., Berghaeuser, G. & Malic, E. Exciton relaxation cascade in two-dimensional transition metal dichalcogenides. *Sci. Rep.* **8**, 1–8 (2018).
46. Cocchi, C., Breuer, T., Witte, G. & Draxl, C. Polarized absorbance and Davydov splitting in bulk and thin-film pentacene polymorphs. *Phys. Chem. Chem. Phys.* **20**, 29724–29736 (2018).
47. Thompson, J. J. P. et al. Singlet-exciton optics and phonon-mediated dynamics in oligoacene semiconductor crystals. *Natural Sci.* **3**, e20220040 (2022).
48. Perea-Causín, R., Brem, S. & Malic, E. Microscopic modeling of pump–probe spectroscopy and population inversion in transition metal dichalcogenides. *Phys. Status Solidi B* **257**, 2000223 (2020).

49. Katsch, F., Selig, M. & Knorr, A. Theory of coherent pump–probe spectroscopy in monolayer transition metal dichalcogenides. *2D Mater.* **7**, 015021 (2019).
50. Selig, M. et al. Ultrafast dynamics in monolayer transition metal dichalcogenides: interplay of dark excitons, phonons, and intervalley exchange. *Phys. Rev. Res.* **1**, 022007 (2019).
51. Claus F. Klingshirn. Semiconductor Optics. Springer Science & Business Media (2012).
52. Usman, A. et al. Enhanced excitonic features in an anisotropic ReS_2/WSe_2 heterostructure. *Nanoscale* **14**, 10851–10861 (2022).
53. Zhao, W.-L., Li, M., Lu, H.-Y. & Chen, C.-F. Advances in helicene derivatives with circularly polarized luminescence. *Chem. Commun.* **55**, 13793–13803 (2019).
54. Perea-Causin, R. et al. Exciton optics, dynamics, and transport in atomically thin semiconductors. *APL Mater.* **10**, 100701 (2022).
55. Sharifzadeh, S. Many-body perturbation theory for understanding optical excitations in organic molecules and solids. *J. Phys. Condens. Matter* **30**, 153002 (2018).
56. Alvertis, A. M. et al. Impact of exciton delocalization on exciton-vibration interactions in organic semiconductors. *Phys. Rev. B* **102**, 081122 (2020).
57. Thorsmølle, V. K. et al. Morphology effectively controls singlet-triplet exciton relaxation and charge transport in organic semiconductors. *Phys. Rev. Lett.* **102**, 017401 (2009).
58. Wang, G. et al. In-plane propagation of light in transition metal dichalcogenide monolayers: optical selection rules. *Phys. Rev. Lett.* **119**, 047401 (2017).
59. Pati, Y. A. & Ramasesha, S. Exact solution of the PPP model for correlated electronic states of tetracene and substituted tetracene. *J. Phys. Chem. A* **118**, 4048–4055 (2014).
60. Zeng, H., Dai, J., Yao, W., Xiao, D. & Cui, X. Valley polarization in MoS2 monolayers by optical pumping. *Nat. Nanotechnol.* **7**, 490–493 (2012).
61. Camposeo, A. et al. Polarized superradiance from delocalized exciton transitions in tetracene single crystals. *Phys. Rev. B* **81**, 033306 (2010).

ACKNOWLEDGEMENTS

This project has received funding from Deutsche Forschungsgemeinschaft via CRC 1083 and the European Unions Horizon 2020 research and innovation programme under grant agreement no. 881603 (Graphene Flagship).

AUTHOR CONTRIBUTIONS

E.M. conceived the project. J.J.P.T. developed the theory and performed the calculations. E.M., J.J.P.T., M.G. and G.W. analyzed the obtained results. J.J.P.T. wrote the paper with all the authors contributing to the discussion and preparation of the manuscript.

FUNDING

Open Access funding enabled and organized by Projekt DEAL.

COMPETING INTERESTS

The authors declare no competing interests.

ADDITIONAL INFORMATION

Supplementary information The online version contains supplementary material available at https://doi.org/10.1038/s41699-023-00430-z.

Correspondence and requests for materials should be addressed to Joshua J. P. Thompson.

Reprints and permission information is available at http://www.nature.com/reprints

Publisher's note Springer Nature remains neutral with regard to jurisdictional claims in published maps and institutional affiliations.